Asian Journal of Chemistry; Vol. 38, No. 7 (2026), 1816-1824
ASIAN JOURNAL OF CHEMISTRY
https://doi.org/10.14233/ajchem.2026.36190

Bougainvillea glabra-Mediated ZnO/rGO Nanocomposite for Enhanced Photocatalytic Degradation of Methylene Blue and Antibacterial Activity

K. SUJITHA[1,2,*], K. BALAKRISHNAN[1], N. MANI[1], S. JOTHI RAMALINGAM[1], S. SASIKRUBA[3] and P. DHARSHINI[2]

[1]PG and Research Department of Chemistry, A.V.V.M. Sri Pushpam College (Autonomous) (Affiliated to Bharathidasan University, Tiruchirappalli), Poondi-613502, India
[2]Department of Chemistry, Sengamala Thayaar Educational Trust Women's College (Autonomous) (Affiliated to Bharathidasan University, Tiruchirappalli), Sundarakkottai, Mannargudi-614016, India
[3]Department of Chemistry, Tagore Engineering College, Rathinamangalam, Vandalur, Chennai-600127, India

*Corresponding author: E-mail: ssujithatvr@gmail.com

Received: 9 April 2026 *Accepted*: 1 June 2026 *Published online*: 3 July 2026 AJC-22407

The synthesised ZnO/rGO/*Bougainvillea glabra* nanocomposite demonstrates significant structural and functional modifications due to the incorporation of rGO and plant-derived phytochemicals. A reduction in crystallite size from 28.8 nm to 2-4 nm indicates controlled nucleation and growth during synthesis. Fourier-transform infrared spectroscopy (FTIR) analysis confirms Zn–O bonding along with organic functional groups, evidencing surface modification by plant extract. Morphological analysis reveals a heterogeneous structure, contributing to increased active surface area. The band gap reduction from 3.29 to 3.18 eV suggests enhanced light absorption, likely due to ZnO–rGO interactions facilitating improved electron transfer. Photocatalytic studies show enhanced methylene blue degradation compared to pristine ZnO, attributed to efficient charge separation and reduced electron–hole recombination. The composite retains activity over multiple cycles, indicating good stability. The synthesized nanocomposite also exhibited modest antibacterial activity against the tested bacterial strains, which may be attributed to reactive species generation and surface interactions.

Keywords: ZnO, Reduced graphene oxide, *Bougainvillea glabra*, Photocatalysis, Methylene blue, Antibacterial activity.

INTRODUCTION

The rapid expansion of industrial activities, particularly in the textile, pharmaceutical and dye-manufacturing sectors, has resulted in the continuous discharge of organic pollutants into aquatic environments. Synthetic dyes represent a major class of these contaminants owing to their extensive production and widespread use. During industrial processing, a significant fraction of dyes is released into wastewater streams, where their complex molecular structures and high stability hinder natural degradation. Dyes such as methylene blue, methyl orange, malachite green and rhodamine B have been widely investigated due to their persistence and potential adverse effects on aquatic ecosystems and human health [1-4]. Conventional treatment methods including adsorption, coagulation, membrane filtration and biological processes, have been employed for dye removal; however, these techniques often suffer from limitations such as incomplete degradation and the generation of secondary waste [5-7]. Consequently, advanced oxidation processes (AOPs), particularly heterogeneous photocatalysis, have emerged as promising alternatives for wastewater treatment.

Photocatalysis involves the excitation of semiconductor materials under light irradiation, generating electron–hole pairs that subsequently produce reactive oxygen species capable of degrading organic pollutants [8-10]. Semiconductor materials such as ZnO, TiO_2, SnO_2, CdS and WO_3 have been extensively explored for photocatalytic applications owing to their favourable physico-chemical properties [11-14]. Among these materials, ZnO has emerged as a widely investigated photocatalyst owing to its abundance, low toxicity, environmental friendliness and suitable electronic characteristics. However, its practical application is limited by a wide band gap, rapid electron–hole recombination, photocorrosion and poor visible-light utilization [15-19].

To overcome these limitations, several modification strategies, including doping, heterojunction construction, and composite formation, have been investigated. In particular,

This is an open access journal, and articles are distributed under the terms of the Attribution 4.0 International (CC BY 4.0) License. This license lets others distribute, remix, tweak, and build upon your work, even commercially, as long as they credit the author for the original creation. You must give appropriate credit, provide a link to the license, and indicate if changes were made.

reduced graphene oxide (rGO) has gained interest because of its high surface area and excellent electrical conductivity, which can facilitate charge transfer and suppress charge-carrier recombination in semiconductor systems [20]. Similarly, heterostructured composites such as ZnO/CdS and ZnO/TiO_2 have demonstrated improved photocatalytic performance through enhanced interfacial charge transfer and light absorption properties [21,22].

Green synthesis using plant extracts has recently emerged as an ecofriendly approach for nanomaterial preparation. Plant-derived phytochemicals, including flavonoids, alkaloids, phenolics and proteins, can act as reducing and stabilizing agents during nanoparticle synthesis [23,24]. Extensive studies have reported the successful preparation of metal oxide nanomaterials using plant extracts, resulting in materials with diverse structural and functional properties [25]. In addition to photocatalytic applications, ZnO-based materials have been widely studied for antibacterial activity, which has been attributed to reactive oxygen species generation, metal ion release and interactions with microbial cell membranes [26]. The performance of photocatalytic systems is strongly influenced by operational parameters such as solution pH, initial dye concentration and catalyst dosage [27,28]. Moreover, characterisation techniques including XRD, FTIR, UV-visible spectroscopy and SEM provide valuable information regarding the structural, morphological and optical properties of nanomaterials and their relationship to functional performance.

In present study, ZnO/rGO/*Bougainvillea glabra* nanocomposites were synthesized *via* a green, plant-mediated route utilizing the phytochemical constituents of *B. glabra* extract. The influence of rGO incorporation and plant-derived components on the structural, optical, photocatalytic, recyclability, and antibacterial properties of the synthesized nanocomposite was systematically investigated. The photocatalytic performance was evaluated through methylene blue degradation under different experimental conditions, while recyclability and antibacterial studies were conducted to assess the stability and environmental applicability of the material.

EXPERIMENTAL

Zinc sulphate heptahydrate ($ZnSO_4 \cdot 7H_2O$), ethanol, sodium hydroxide, potassium permanganate, ascorbic acid, sulphuric acid, phosphoric acid, hydrogen peroxide (30 wt.%), methylene blue and all other analytical-grade chemicals and solvents were used as received from Merck Ltf., India and were used without further purification. Fresh flowers of *Bougainvillea glabra* were collected and used for the extract preparation. Graphene oxide (GO) and zinc oxide (ZnO) were employed for nanocomposites synthesis.

Synthesis of ZnO nanoparticles: A precursor solution of $ZnSO_4 \cdot 7H_2O$ was prepared in deionized water and stirred continuously. Sodium hydroxide solution was added dropwise to the precursor solution under constant stirring until a homogeneous sol was formed. The reaction mixture was maintained at 50-60 ºC, leading to the formation of a thick whitish gel. The resulting gel was washed repeatedly with deionized water and ethanol to remove residual impurities, followed by drying in an oven at 100-120 ºC. The dried product was ground into a fine powder and calcined at 400-600 ºC for several hours to obtain ZnO nanoparticles.

Synthesis of rGO: Graphene oxide (GO) was synthesised from graphite powder through chemical oxidation using $KMnO_4$ in a mixed H_2SO_4/H_3PO_4 medium (9:1, v/v) at 50 ºC for 12 h. The resulting graphite oxide was dispersed in deionized water and stirred at 60 ºC for 12 h to achieve exfoliation, followed by filtration, centrifugation, and drying at 60 ºC for 24 h to obtain GO [29]. For the preparation of reduced graphene oxide (rGO), GO (400 mg) was dispersed in distilled water (400 mL) and treated with ascorbic acid (4 g) as a reducing agent. The mixture was stirred at 60 ºC for 30 min, and the resulting product was collected by centrifugation at 4000 rpm for 40 min. Residual ascorbic acid was removed by treatment with 30 wt.% H_2O_2 under continuous stirring at 60 ºC for 30 min. The product was then centrifuged, washed repeatedly with ethanol and distilled water and dried at 120 ºC for 24 h to afford rGO.

Preparation of *B. glabra* flowers extract: Collected fresh *B. glabra* flowers were thoroughly washed with deionsed water, shade-dried at room temperature and ground into a fine powder. The powdered material (5-10 g) was mixed with 100 mL of deionsed water and heated at 60-80 ºC for 20-30 min under continuous stirring. The resulting extract was filtered through Whatman No. 1 filter paper and the clear filtrate was collected and stored at 4 ºC for subsequent use in nanocomposite synthesis.

Synthesis of ZnO/rGO/*B. glabra* nanocomposite: rGO was dispersed in distilled water and sonicated for 30-60 min to obtain a uniform suspension. Zinc sulphate was then added under continuous stirring, followed by the slow addition of *B. glabra* flower extract. The reaction mixture was maintained at 60-80 ºC with constant stirring, facilitating the simultaneous reduction of GO and formation of ZnO nanoparticles. The pH of the mixture was adjusted with NaOH, when necessary and stirring was continued until precipitation occurred. The resulting precipitate was collected by centrifugation, washed thoroughly with distilled water and ethanol and dried at 60-80 ºC. The dried material was subsequently calcined at 400-500 ºC for 2-3 h to afford ZnO/rGO/*B. glabra* nanocomposites containing 1, 3, 5, and 7 wt.% rGO. Graphene oxide (GO) was dispersed in distilled water and sonicated for 30-60 min to obtain a uniform suspension. Zinc sulphate was then added to the GO suspension under continuous stirring to form a homogeneous solution. The *B. glabra* flower extract was added slowly and the mixture was maintained at 60-80 ºC under stirring. During this process, reduction of GO and formation of ZnO nanoparticles occurred simultaneously. The reaction mixture was further stirred until precipitation was observed. The pH was adjusted using NaOH, if required. The precipitate was collected by centrifugation, washed with distilled water and ethanol and dried at 60-80 ºC. Finally, the dried product was calcined at 400-500 ºC for 2-3 h to obtain the 1%, 3%, 5% and 7% ZnO/rGO/*B. glabra* nanocomposites.

Photocatalytic activity: The photocatalytic degradation of methylene blue (MB) dye was studied using ZnO/rGO/*B. glabra* nanocomposites with different weight percentages (1% 3%, 5% and 7% under UV-A light (λ = 365 nm and an intensity of 10 mW/cm^2). Among them, 1 wt.% ZnO/rGO/*B.*

glabra catalyst exhibited the highest degradation efficiency due to its optimal balance of active sites, enhanced light absorption and improved charge separation. In contrast, lower loadings (3% and 5%) showed reduced activity, while the 7 wt.% sample displayed decreased performance, likely due to ZnO/-rGO/*B. glabra* aggregation and increased charge recombination. When compared to pure ZnO, which achieved 79% degradation under UV-A light, the 1 wt.% ZnO/rGO/*B. glabra* nanocomposite showed a superior 89% degradation efficiency as shown in Fig. 1.

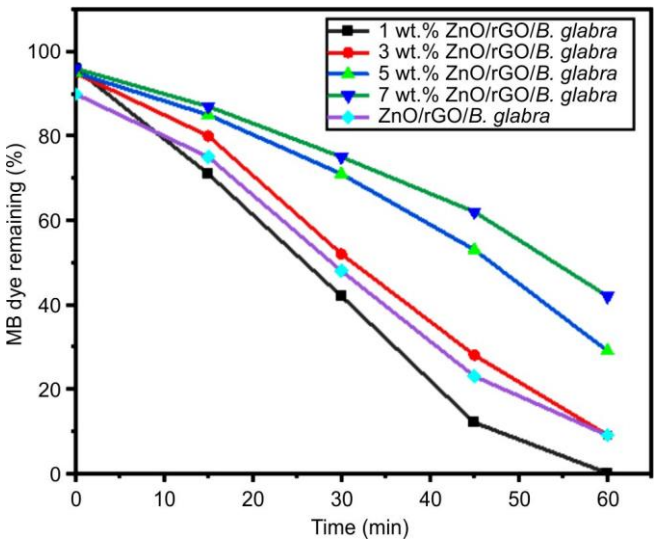

Fig. 1. Photodegradation of MB with ZnO/rGO/*B. glabra* catalysts under UV-light. [MB] = 4×10^{-4} M, airflow rate = 8.1 mL s^{-1}, pH = 7.0, $I_{UV} = 1.381 \times 10^{-6}$ mol photons L^{-1} s^{-1}

To evaluate the photocatalytic activity, 20 mg of each nanocomposite was added to 100 mL of 20 mg/L MB dye solution and stirred in dark for 30 min to ensure equilibrium adsorption. The mixture was then irradiated under UV-A light for 60 min and degradation was monitored by measuring absorbance at 640 nm and 515 nm. The catalysts also demonstrated good reusability, retaining performance over multiple cycles, indicating their potential for long-term wastewater treatment. Based on the promising results with 1 wt.% ZnO/rGO/*B. glabra*, further characterisation studies were carried out to better understand its structure property relationship and photocatalytic mechanism. The degradation efficiency was calculated using eqn. 1:

$$\text{Degradation (\%)} = \frac{C_o - C_t}{C_t} \times 100 \quad (1)$$

where C_o = initial concentration, C_t = concentration at time t.

Characterisation: XRD analysis was performed using an ARL EQUINOX 3000 with Cu*K*α radiation over a 2θ range of 0-120º, based on Bragg's law, to examine the crystalline structure and phase composition of the samples. FTIR analysis was carried out using a JASCO FT/IR-6600 over a wavenumber range of 4800-350 cm^{-1} to identify functional groups and analyze the chemical composition of the samples. FESEM analysis was performed using a Carl Zeiss Sigma 300 to examine surface morphology, while EDS was employed for elemental composition analysis of the samples. UV–Vis–NIR analysis was performed using a JASCO V-670 over a wavelength range of 190-2700 nm to evaluate the optical properties and absorption characteristics of the samples. Antibacterial activity was tested by agar well diffusion at 10-200 µg/mL. The zones of inhibition were measured after incubation at 37 ºC for 24 h using appropriate positive and negative controls.

RESULTS AND DISCUSSION

XRD studies: The XRD patterns were studied for ZnO, ZnO/rGO, *B. glabra* and ZnO/rGO/*B. glabra* samples to observe their structural features. The diffraction pattern of ZnO shows reflections at 2θ values of 31.9º, 34.4º, 36.2º, 47.6º, 56.2º, 63.0º, 67.6º and 89.2º, which are associated with the planes (100), (002), (101), (102), (110), (103), (112) and (203) is shown in Fig. 2. These reflections correspond to the hexagonal Wurtzite structure phase reported for ZnO (JCPDS card No. 96-210-7060). The PXRD pattern of pure ZnO exhibited well-defined diffraction peaks characteristic of a crystalline hexagonal wurtzite structure. The prominent (002) reflection at 2θ = 34.4º showed relatively high intensity, suggesting preferential growth along the *c*-axis. The calculated crystallite size was approximately 28.8 nm, while the *d*-spacing and dislocation density values were determined to be 1.92 Å and 873.618, respectively, providing insight into the lattice arrangement and defect distribution within the ZnO framework.

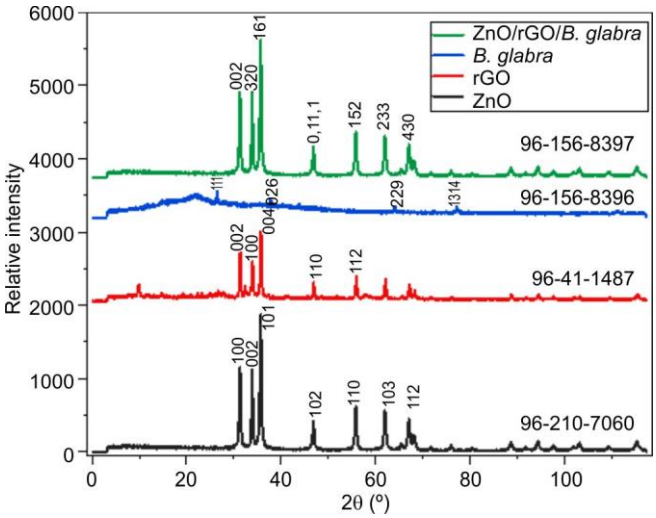

Fig. 2. XRD patterns of ZnO, rGO, *B. glabra*, 1 wt.% of ZnO/rGO/*B. glabra*

For the ZnO/rGO composite, diffraction peaks were observed at 2θ values of 24.8º, 26.4º, 42.6º, 44.3º and 54.5º. The reflection near 26.4º corresponds to the (002) plane of reduced graphene oxide (rGO), confirming the successful incorporation of rGO sheets into the composite. The remaining peaks are attributed to crystalline ZnO, indicating that the ZnO crystal structure was retained after rGO incorporation. Compared with pure ZnO, the diffraction peaks became broader, suggesting a reduction in crystallite size and enhanced interaction between ZnO nanoparticles and rGO sheets.

The PXRD pattern of powdered *B. glabra* displayed diffraction peaks at 2θ values of 26.40º, 38.22º, 64.55º and

77.21º. The broad nature of these reflections, together with a *d*-spacing value of 0.84 nm, is characteristic of partially ordered regions present in plant-derived constituents such as cellulose, lignin and other phytochemicals. The estimated crystallite size of 16.89 nm further indicates the presence of nanoscale ordered domains within the plant matrix.

The ZnO/rGO/*B. glabra* nanocomposite exhibited diffraction peaks at 31.27º, 33.88º, 46.83º, 55.80º, 62.01º and 67.03º, corresponding to crystalline ZnO planes and confirming the preservation of the ZnO lattice in the final composite. The calculated *d*-spacing values ranged from 0.286 to 0.139 nm, while the crystallite size decreased significantly to approximately 2-4 nm. This reduction in crystallite size may be attributed to the synergistic effect of rGO sheets and *B. glabra* phytoconstituents, which likely restricted the crystal growth during synthesis. The dislocation density values (0.075-0.186 nm^{-2}) indicate the presence of lattice imperfections that can influence the physico-chemical properties of the material. Thus, the PXRD analysis confirms the coexistence of ZnO, rGO, and *B. glabra*-derived components within the ZnO/rGO/*B. glabra* composite. The presence of characteristic reflections associated with ZnO, together with features attributable to rGO and plant constituents, provides strong evidence for the successful formation of the nanocomposite, as summarized in Table-1.

Microstructural characterization: The morphological and microstructural features of the synthesized ZnO/rGO/*B. glabra* nanocomposite were examined using TEM, HRTEM, and SAED analyses. The TEM image (Fig. 3a) revealed densely packed nanostructures with irregular morphology and agglomeration, likely arising from interactions between ZnO nanoparticles and rGO nanosheets. Regions with higher contrast were attributed to ZnO nanoparticles, whereas the relatively transparent and layered features corresponded to rGO sheets, indicating the successful incorporation of ZnO within the graphene-based matrix.

Higher-magnification TEM micrograph (Fig. 3b) showed predominantly irregular and quasi-spherical ZnO nanoparticles anchored onto the rGO sheets. Although some degree of agglomeration was observed, the particles remained distributed within the nanometer scale, confirming the formation of a nanosized hybrid composite. The close association between ZnO nanoparticles and rGO sheets suggests effective interfacial contact within the composite structure. Moreover, the HRTEM images exhibited well-resolved lattice fringes, confirming the crystalline nature of the nanocomposite. The measured interplanar spacings of 0.437, 0.550, 0.487 and 0.287 nm were indexed to the (111), (203), (112) and (111) crystallographic planes, respectively, indicating the presence of ordered crystalline domains. These lattice fringes further verify the successful crystallization of ZnO within the hybrid framework. The SAED pattern (Fig. 3c) displayed a series of concentric diffraction rings accompanied by discrete bright spots, characteristic of a polycrystalline material. The presence of these diffraction rings indicates multiple randomly oriented crystalline domains distributed throughout the composite matrix.

FTIR: The FTIR spectra of ZnO, rGO, *B. glabra* extract, and the ZnO/rGO/*B. glabra* nanocomposite were recorded in the range of 4000-400 cm^{-1} and are shown in Fig. 4. The observed absorption bands provide information about the functional groups present in the individual components as well as their interactions within the composite. The FTIR spectrum of *B. glabra* showed a broad band around 3450 cm^{-1}, which can be attributed to O–H stretching vibrations of hydroxyl-containing phytochemicals. The absorption band at

TABLE-1
STRUCTURAL PARAMETERS INCLUDING AVERAGE d-SPACING, CRYSTALLITE SIZE FACTOR (D^2) AND FULL WIDTH AT HALF MAXIMUM (FWHM, β) OBTAINED FROM XRD ANALYSIS OF ZnO, rGO AND ZnO/rGO-BASED NANOCOMPOSITES

Sample	B = FWHM X π/180	Crystallite size (nm)	D^2	*d*-spacing (nm)
ZnO	0.33925	28.8125	873.61875	1.92625
ZnO/rGO	0.24	4.64	21.98	0.256
B. glabra	0.004858	3.82	16.89923	0.84
ZnO/rGO/*B. glabra*	0.0057764	2.773	7.8953	0.199

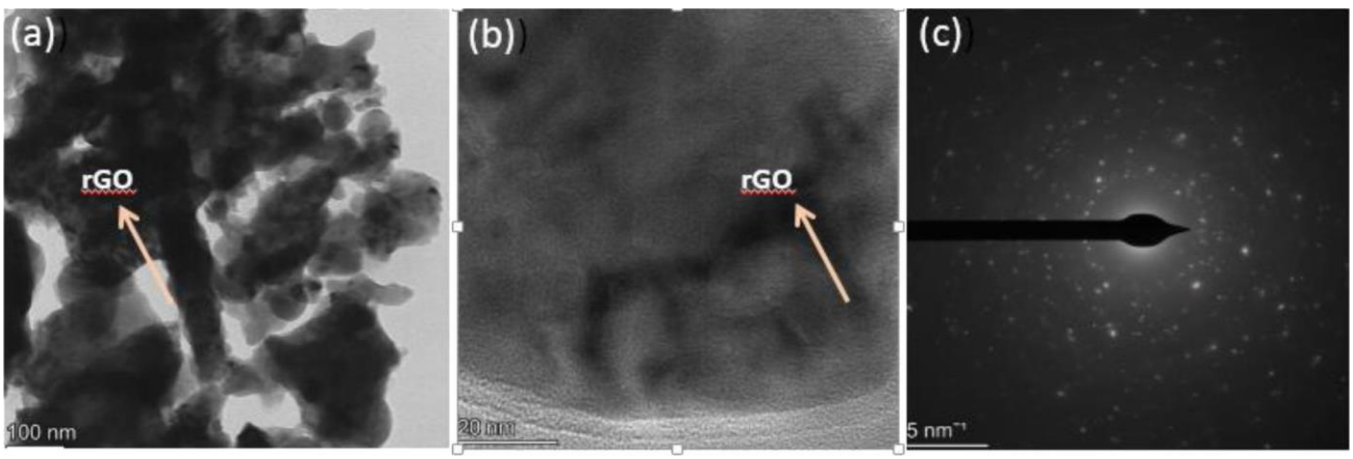

Fig. 3. (a) TEM, (b) HRTEM and (c) SAED images of 1 wt.% ZnO/rGO/*B. glabra* nanocomposite

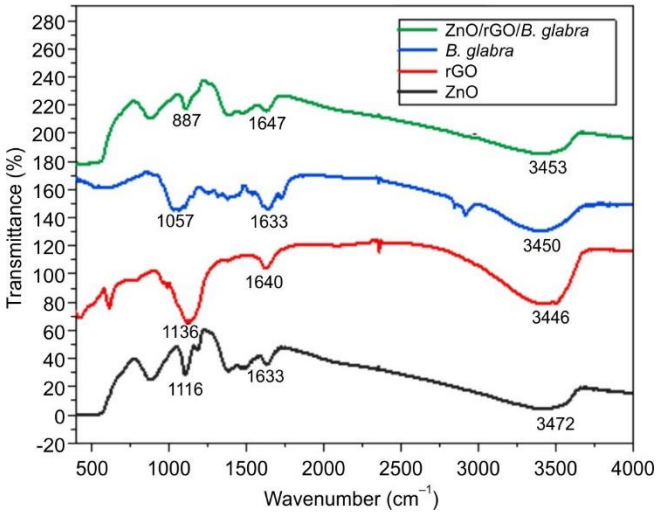

Fig. 4. FTIR spectra of ZnO, rGO, *B. glabra*, 1 wt.% of ZnO/rGO/*B. glabra*

1057 cm^{-1} is assigned to C–O stretching vibrations, while the peak near 1633 cm^{-1} corresponds to C=O and/or C=C stretching vibrations. In the rGO spectrum, bands observed at ~ 3446 and 1640 cm^{-1} indicate the presence of residual oxygen containing functional groups, such as hydroxyl and carbonyl groups, remaining after the reduction process. The ZnO spectrum exhibited characteristic bands at 3472, 1633 and 1116 cm^{-1}. The broad absorption near 3472 cm^{-1} is due to the hydroxyl groups present on the surface, whereas the band around 1633 cm^{-1} may arise from adsorbed water molecules. The Zn–O stretching vibration is generally expected below 500 cm^{-1} and appears near the lower limit of the recorded spectral range.

For ZnO/rGO/*B. glabra* nanocomposite, the absorption bands were observed at approximately 3453, 1647, 887 and 510 cm^{-1}. The bands at 3453 and 1647 cm^{-1} reflect the presence of hydroxyl and carbonyl containing groups contributed by both rGO and *B. glabra* components, while the band at 510 cm^{-1} confirms the presence of Zn–O bonds. Compared with the individual constituents, slight shifts in peak positions and variations in band intensities were observed in the nanocomposite spectrum. These changes suggest interactions between ZnO nanoparticles, rGO sheets and phytochemical constituents of *B. glabra*. At the same time, the retention of the major characteristic bands indicates that the fundamental chemical structures of the individual components remain preserved after composite formation. These findings support the successful synthesis of the ZnO/rGO/*B. glabra* nanocomposite.

Morphological studies: SEM micrographs of 1 wt.% ZnO/*B. glabra* sample recorded at different magnifications reveal a surface composed of irregularly distributed and aggregated structures. At higher magnification (Fig. 5), the agglomerated structures were found to be composed of smaller granular particles, resulting in a rough and uneven surface texture. The particles exhibited irregular morphology with observable variations in size and shape throughout the examined region. While some areas appeared densely packed, others showed a relatively loose arrangement of particles. No clear long-range ordering or well-isolated individual particles were observed, suggesting strong particle–particle interactions within the composite matrix.

The elemental composition was further examined by EDAX analysis. The spectrum confirmed the presence of Zn

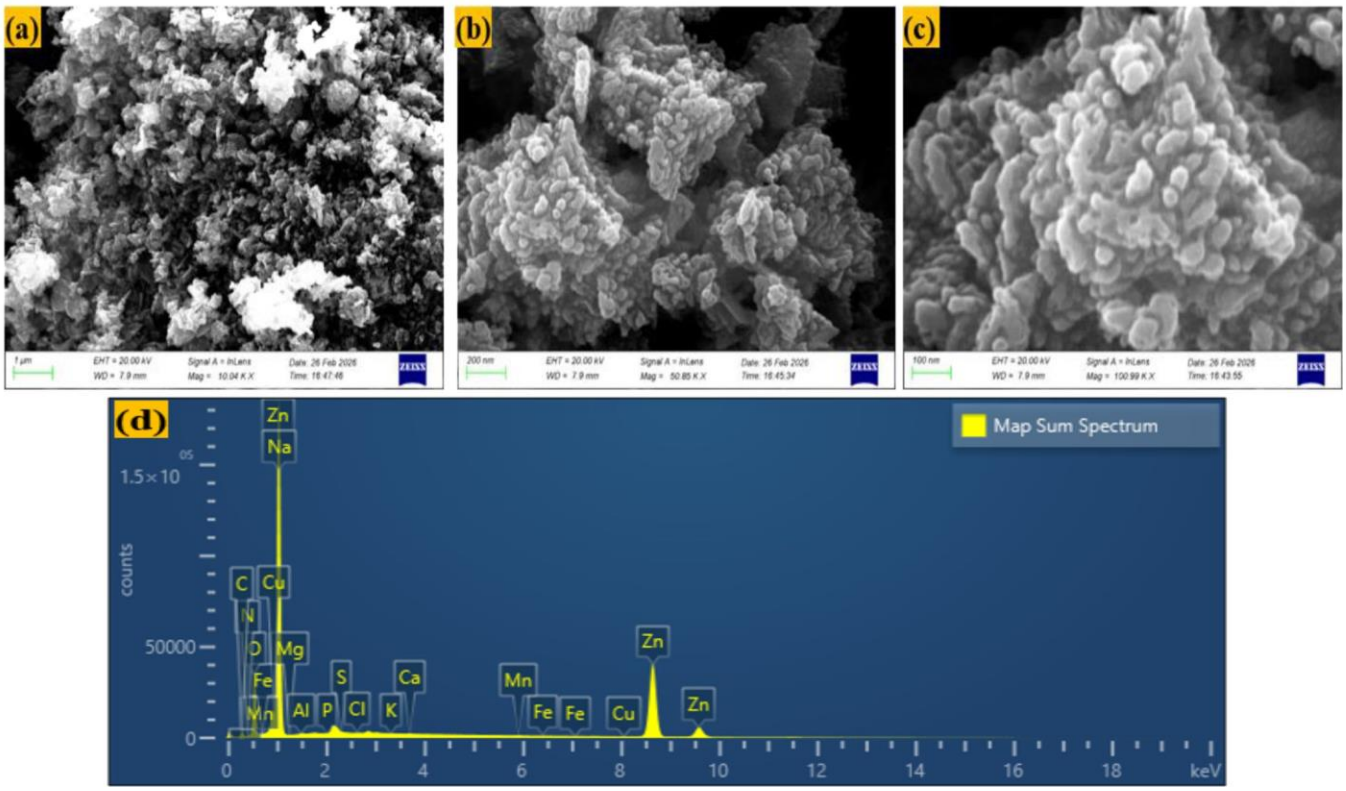

Fig. 5. (a-c) SEM images and (d) EDX spectrum of 1 wt.% ZnO/rGO/*B. glabra* nanocomposite

and O as the predominant elements, along with significant amounts of C and Na. Additional elements, including Al, Ca, Mn, and Fe, were also detected but with comparatively lower intensities. The relatively strong signals of Zn, O, and C indicate that these elements constitute the major components of the material, whereas the remaining elements are present in minor quantities. However, variations in the elemental peak intensities across the analyzed region suggest differences in local elemental distribution. The SEM and EDAX results together reveal a heterogeneous composite structure containing multiple elements distributed throughout the surface, although their distribution is not entirely uniform.

UV-DRS: The UV–visible diffuse reflectance spectra (UV–DRS) of ZnO, ZnO/rGO and ZnO/rGO/*B. glabra* samples were recorded over the wavelength range of 200-800 nm and the corresponding spectra are shown in Fig. 6. All samples exhibit absorption in the ultraviolet region with a gradual decrease in intensity toward the visible region. The absorption edge of ZnO is observed around ~380-390 nm. In case of ZnO/rGO, a slight shift in the absorption edge toward a longer wavelength region can be observed when compared with ZnO. The ZnO/rGO/*B. glabra* sample shows a further extension of the absorption edge into the visible region along with a comparatively broader absorption profile.

The calculated band gap values were found to be 3.29 eV for ZnO, 3.26 eV for ZnO/rGO and 3.18 eV for ZnO/rGO/*B. glabra*. A gradual variation in the band gap values is observed among the samples, which is reflected in the corresponding shift in the absorption edge positions. The differences in the spectral features and band gap values indicate changes in the optical absorption characteristics of the materials. The ZnO/rGO/*B. glabra* nanocomposite exhibits a relatively reduced band gap and a visible shift of the absorption edge toward the visible region, reflecting an altered optical absorption behaviour that may have implications for photocatalytic performance.

Antibacterial assay: The antibacterial activity of the 1 wt.% ZnO/rGO/*B. glabra* nanocomposite was evaluated against *Staphylococcus aureus* and *Pseudomonas aeruginosa* using the agar well diffusion method. For *S. aureus*, the control exhibited a zone of inhibition of 3.3 mm. No inhibitory effect was observed at concentrations of 10 and 100 μg/mL, whereas a zone of 2 mm was recorded at 200 μg/mL. Similarly, for *P. aeruginosa*, the control produced a zone of inhibition of 3.3 mm. No inhibition was detected at 10 μg/mL, while zones of 2 mm were observed at both 100 and 200 μg/mL (Table-2). The results indicate that the antibacterial activity of the composite is concentration-dependent, with inhibitory effects becoming evident only at higher concentrations. Although the observed inhibition zones were smaller than those of the control, the formation of measurable zones at elevated concentrations demonstrates the ability of the ZnO/rGO/*B. glabra* composite to suppress bacterial growth under the investigated conditions. The nanocomposite demonstrated antibacterial activity against both Gram-positive (*S. aureus*) and Gram-negative (*P. aeruginosa*) bacteria, although the observed inhibition zones were relatively modest under the studied conditions. The inhibition at higher concentrations suggests that the antibacterial effect is the concentration-dependent.

TABLE-2
MINIMUM BACTERIALCIDIAL ACTIVITY DATA

Organism	NC (mm)	10 μg/mL (mm)	100 μg/mL (mm)	200 μg/mL (mm)
Staphylococcus aureus	3.3	–	–	2
Pseudomonas aeruginosa	3.3	–	2	2

NC = ZnO/rGO/*B. glabra* nanocomposite

UV-A Photodegradation of methylene blue (MB) by 1 wt.% ZnO/rGO/*B. glabra*: Parameter effects

Influence of pH: The photocatalytic degradation of MB using the ZnO/rGO/*B. glabra* nanocomposite was studied at different pH conditions (pH 4-8) and the corresponding profiles are shown in Fig. 7. At the initial stage, the percentage of dye remaining is observed within a comparable range for all pH conditions. With increasing irradiation time, a decrease in dye concentration is observed across the studied pH range.

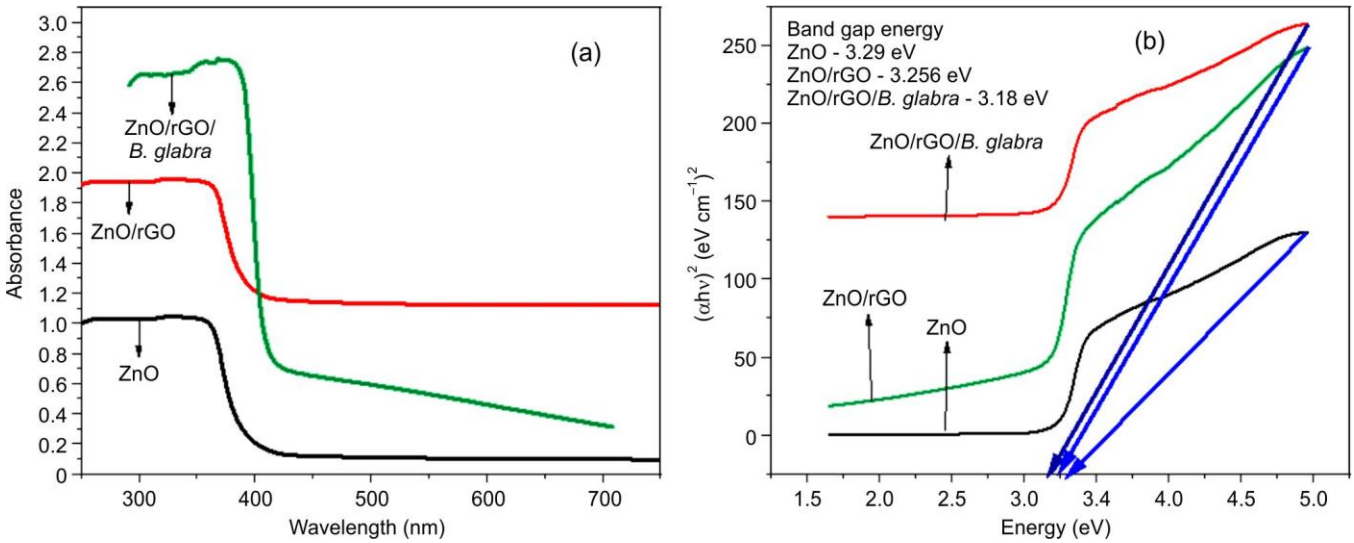

Fig. 6. (a) UV-DRS spectra (a) and band gap energy plots (b) of ZnO and ZnO/rGO and 1 wt.% ZnO/rGO/*B. glabra* nanocomposites

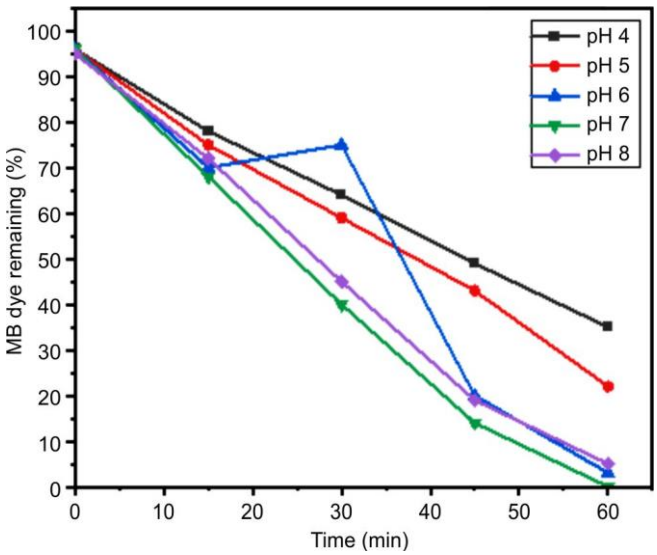

Fig. 7. Influence of pH on UV-A degradation [MB] = 4×10^{-4} M, 1 wt.% ZnO/rGO/*B. glabra* = 2 g L^{-1}, airflow rate = 8.1 mL s^{-1}, irradiation time = 60 min, $I_{UV} = 1.381 \times 10^{-6}$ mol photons L^{-1} s^{-1}

The extent of change varies at different time intervals for each pH condition. At pH 4 and 5, the reduction in dye concentration proceeds gradually over the irradiation period. For pH 6, 7 and 8, the dye concentration decreased progressively with increasing irradiation time, confirming the occurrence of photocatalytic degradation under all tested conditions. Although a similar declining trend was observed at each pH, differences in the extent of dye removal were evident. Among the investigated conditions, pH 7 exhibited the most effective degradation performance and was therefore considered the optimum pH for photocatalytic degradation under the present experimental conditions.

Effect of catalyst loading: The effect of catalyst dosage on the photocatalytic degradation of MB dye was investigated by varying the catalyst amount from 50 to 150 mg, and the results are shown in Fig. 8. A progressive decrease in dye concentration with increasing irradiation time was observed for all catalyst dosages, confirming the photocatalytic activity of the material. However, at a catalyst loading of 50 mg, the degradation process was relatively slow, resulting in a higher percentage of residual dye after 60 min. Increasing the dosage to 75 mg and 100 mg enhanced the degradation efficiency, as evidenced by the greater reduction in dye concentration over the irradiation period. Among the tested dosages, 100 mg exhibited the lowest residual dye concentration at most time intervals indicating improved photocatalytic performance. A similar trend was observed at 125 mg, where the dye concentration continued to decrease steadily and reached a low residual level after 60 min.

When the catalyst dosage was further increased to 150 mg, degradation still occurred; however, the reduction in dye concentration was less pronounced at certain intermediate time intervals compared with the 100 and 125 mg loadings. This behaviour may be attributed to changes in the availability of active sites and reduced light penetration caused by excess catalyst particles in the reaction medium. Based on the observed degradation profiles, a catalyst dosage of 100 mg was found to be the most suitable under the experimental conditions.

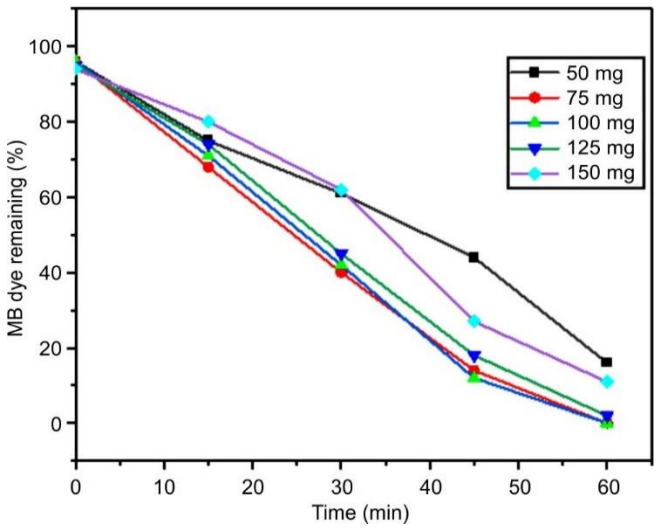

Fig. 8. Influence of catalyst loading on UV-A degradation [MB] = 4×10^{-4} M, 1 wt.% ZnO/rGO/*B. glabra* = 2 g L^{-1}, airflow rate = 8.1 mL s^{-1}, irradiation time = 60 min, $I_{UV} = 1.381 \times 10^{-6}$ mol photons L^{-1} s^{-1}

Effect of concentration: The effect of initial dye concentration on the photocatalytic degradation of MB was investigated by varying the concentration from 2×10^{-5} M to 5×10^{-5} M and the results are shown in Fig. 9. For all concentrations, the percentage of dye remaining decreases with increasing irradiation time, indicating a gradual reduction in dye concentration during the process. At lower dye concentration (2×10^{-5} M), the degradation progresses more rapidly, with a relatively lower percentage of dye remaining at each time interval. As the dye concentration increases to 3×10^{-5} M and 4×10^{-5} M, the reduction in dye concentration with time continues, although a comparatively higher amount of dye remains at intermediate stages. At the highest concentration (5×10^{-5} M), the degradation appears relatively slower, with a higher percentage of dye remaining throughout the reaction period. This trend may be associated with factors such as reduced light penetration and increased competition among dye molecules for available active sites at higher concen-

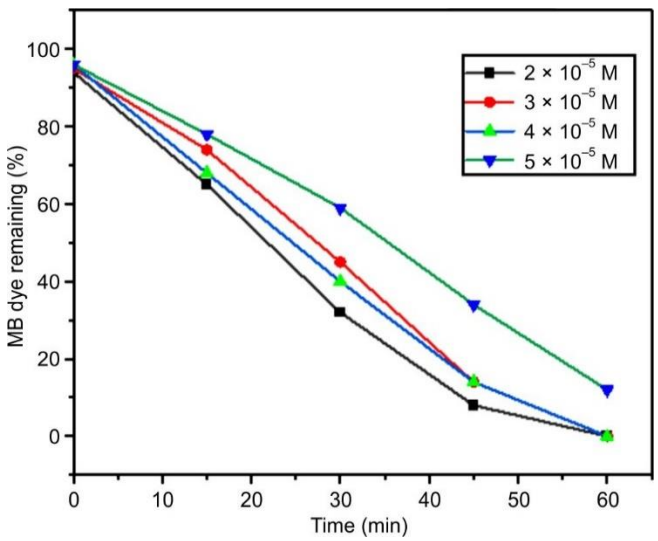

Fig. 9. Influence of dye concentration on UV-A degradation [MB]. 1 wt.% ZnO/rGO/*B. glabra* = 3 g L^{-1}, airflow rate = 8.1 mL s^{-1}, pH = 7.0, irradiation time = 60 min

trations. The lower dye concentration conditions, particularly around 2×10^{-5} M, appear to be more favourable for effective photocatalytic degradation.

Radical scavenger studies: Radical scavenger experiments were conducted to identify the active species involved in the photocatalytic degradation process. The photocatalytic activity without scavengers was considered as 100%. The addition of isopropanol (IPA, $^{\bullet}OH$ scavenger) reduced the degradation efficiency to 28.6%, indicating that hydroxyl radicals are the dominant reactive species. Potassium iodide (h^+ scavenger) decreased the activity to 46.1%, confirming the significant role of photogenerated holes. Benzoquinone ($^{\bullet}O_2^-$ scavenger) reduced the activity to 62.1%, suggesting moderate involvement of superoxide radicals, whereas $AgNO_3$ (e^- scavenger) retained 73.2% activity, indicating a relatively minor contribution of electrons (Fig. 10). The contribution of reactive species followed the order: $^{\bullet}OH > h^+ > {}^{\bullet}O_2^- > e^-$. Thus, hydroxyl radicals were identified as the primary species respon-sible for photocatalytic degradation. However, advanced analyses such as photoluminescence (PL) and electro-chemical impedance spectroscopy (EIS) were not performed, which should be considered a limitation of the present study.

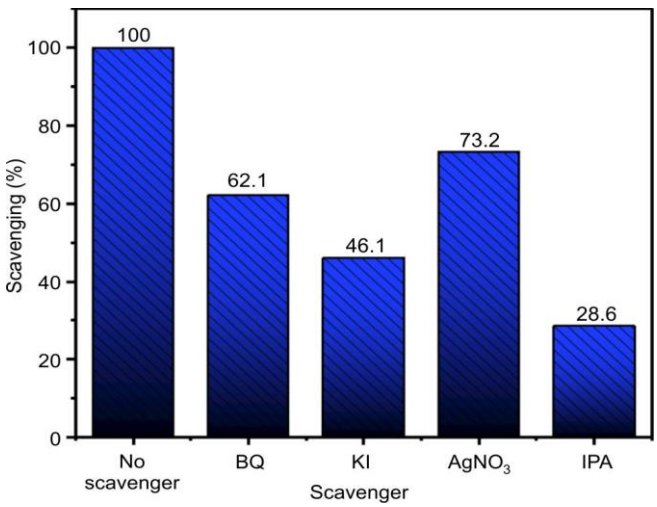

Fig. 10. Effect of radical scavengers on photocatalytic degradation under light irradiation

Reusability: The reusability of the ZnO/rGO/*B. glabra* nanocomposite was evaluated through repeated photocatalytic degradation cycles of MB dye under identical experimental conditions. After each cycle, the catalyst was separated from the reaction mixture, washed and reused for subsequent runs. The degradation percentages recorded for each cycle are presented in Fig. 11. The degradation percentage was 100% during the first cycle, 97% in the second cycle**,** 96% in the third cycle and 93% in the fourth cycle. A variation in degradation percentage is observed across successive cycles. The changes in degradation values are presented with respect to the number of reuse cycles. The data correspond to the measured response of the system under repeated experimental conditions.

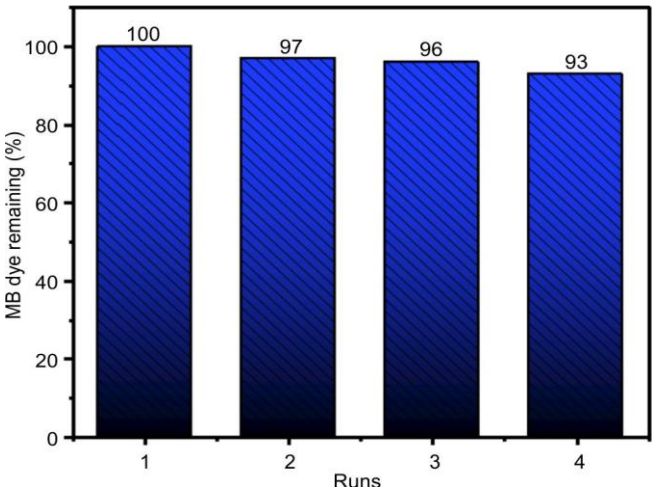

Fig. 11. Influence on reusability on UV-A degradation [MB] = 4×10^{-4} M, 1 wt.% ZnO/rGO/*B. glabra* = 3 g L^{-1}, airflow rate = 8.1 mL s^{-1}, pH = 7.0, irradiation time = 60 min, $I_{UV} = 1.381 \times 10^{-6}$ mol photons L^{-1} s^{-1}

Comparative studies: The comparative analysis with previously reported photocatalytic systems indicates that the ZnO/rGO/*B. glabra* nanocomposite synthesised through the green sol-gel method exhibited 89% methylene blue degradation with a pseudo-first-order rate constant of 0.0368 min^{-1} under the optimized conditions. Differences in photocatalytic performance among the reported studies may be influenced by variations in synthesis procedure, catalyst composition, irradiation source and experimental parameters (Table-3). The present nanocomposite showed reduced crystallite size (2-4 nm) and a band gap value of 3.18 eV, which may be associated with changes in optical behaviour and interfacial interaction within the ZnO/rGO/plant-derived nanocomposite system.

Conclusion

ZnO/rGO/*Bougainvillea glabra* nanocomposites were synthesised through a plant-mediated approach and examined to understand the influence of rGO and plant-derived components on material properties. The structural analysis indicated that the wurtzite phase of ZnO was retained, while a reduction in crystallite size to 2-4 nm reflected controlled growth

TABLE-3
COMPARATIVE PHOTOCATALYTIC DEGRADATION PERFORMANCE OF THE PRESENT ZnO/rGO/*B. glabra* NANOCOMPOSITE AND PREVIOUSLY REPORTED GREEN-SYNTHESISED ZNO- AND RGO-BASED PHOTOCATALYSTS

Catalyst/light/dye/synthesis method	Degradation (%)	Rate constant	Ref.
AgNPs/BgC/visible/MB/rainbow assay	84	Pseudo-first-order; 0.0350 min^{-1}	[30]
ZnO/rGO/UV/MB/hydrothermal	86.6	Pseudo-first-order; 0.0103 min^{-1}	[31]
ZnO/rGO/UV/MB/electrochemical method	66, 96.5 and 99.0	Pseudo-first-order; 0.5030 min^{-1}	[32]
Cu-rGO/ZnO/UV-light/bromophenol blue/hydrothermal	86.2	Pseudo-first-order; 0.0221 min^{-1}	[33]
ZnO/rGO/*B. galabra*/Sol-gel method	89	Pseudo-first-order; 0.0368 min^{-1}	Present work

during synthesis. A shift in optical behaviour was observed through band gap reduction from 3.29 eV to 3.18 eV. Photocatalytic studies under UV-A irradiation showed that the 1 wt.% nanocomposite achieved 89% degradation of methylene blue within 60 min under optimised conditions (pH 7, 100 mg, 2×10^{-5} M), while ZnO showed 79% under similar conditions. The material maintained 93% efficiency after four cycles, indicating stable performance. Antibacterial response was observed against both tested bacterial strains, with a maximum inhibition zone of 2 mm at 200 μg mL^{-1}. The observed structural and functional features suggest the potential of the synthesised nanocomposite for photocatalytic wastewater treatment under laboratory-scale conditions. Further studies involving real wastewater systems and large-scale evaluation are required to assess its practical applicability.

ACKNOWLEDGEMENTS

The authors gratefully acknowledge the Centre for Nanoscience and Nanotechnology (CNSNT), Sathyabama Institute of Science and Technology, Chennai, for providing the necessary facilities to carry out this research.

CONFLICT OF INTEREST

The authors declare that there is no conflict of interests regarding the publication of this article.

DECLARATION OF AI-ASSISTED TECHNOLOGIES

During the preparation of this manuscript, the authors used an AI-assisted tool(s) to improve the language. The authors reviewed and edited the content and take full responsibility for the published work.

REFERENCES

1. P. Kumar, K. Singh, J. Singh, M.K. Talla, S. Ali, R. Chauhan and A. Ranjan, *J. Environ. Eng.*, (2026);
2. S. Dutta, S. Adhikary, S. Bhattacharya, S. Chatterjee, A. Chakraborty, D. Roy, D. Banerjee, A. Ganguly, S. Nanda and P. Rajak, *J. Environ. Manag.*, **353**, 120103 (2024); https://doi.org/10.1016/j.jenvman.2024.120103
3. A. Tkaczyk-Wlizło and K. Mitrowska, *Environ. Sci. Pollut. Res.*, **33**, 9225 (2026); https://doi.org/10.1007/s11356-026-37866-x
4. A. Tkaczyk-Wlizło, K. Mitrowska and A. Posyniak, *Sci. Total Environ.*, **717**, 137222 (2020); https://doi.org/10.1016/j.scitotenv.2020.137222
5. K. Abhisek, S.S. Vhatkar, H.T. Mathew, P. Singh and R. Oraon, *Discover Chem.*, **2**, 41 (2025); https://doi.org/10.1007/s44371-025-00111-4
6. M.A.M. Al-Gheethi, A.N.A. Al-Sahari, A.M.M. Mohamed and A.H.M. Kassim, *Environ. Technol. Innov.*, **25**, 102121 (2022); https://doi.org/10.1016/j.eti.2021.102121
7. M.A. Islam, M.A. Al Mamun, A.F.M.F. Halim, R. Peila and D.O.S. Ramirez, *Environ. Sci. Pollut. Res.*, **31**, 19166 (2024); https://doi.org/10.1007/s11356-024-32454-3
8. F. Zhang, X. Wang, H. Liu, C. Liu, Y. Wan, Y. Long and Z. Cai, *Appl. Sci.*, **9**, 2489 (2019); https://doi.org/10.3390/app9122489
9. A.P. Chowdhury, K.S. Anantharaju, K. Keshavamurthy and S.L. Rokhum, *Int. J. Photoenergy*, **2023**, 9780955 (2023); https://doi.org/10.1155/2023/9780955
10. Z. Khan, M. Kamal, G. U. Rehman, U. Niaz, H. D. Rizqi, J. Jaafar, M. Irfan and A. F. Ismail, *Environ. Eng. Res.*, **31**, 250435 (2026); https://doi.org/10.4491/eer.2025.435
11. O. Ishchenko, V. Rogé, G. Lamblin, D. Lenoble and I. Fechete, *Compt. Rendus Chim.*, **24**, 103 (2021); https://doi.org/10.5802/crchim.64
12. J. Dostanić, D. Lončarević, M. Hadnađev-Kostić and T. Vulić, *Processes*, **12**, 1914 (2024); https://doi.org/10.3390/pr12091914
13. M.A. Wahba, *Discov. Mater.*, **6**, 127 (2026); https://doi.org/10.1007/s43939-026-00585-8
14. H. Wu, L. Liu, S. Wang, N. Zhu, Z. Li, L. Zhao and Y. Wang, *Phys. Chem. Chem. Phys.*, **25**, 25232 (2023); https://doi.org/10.1039/D3CP03391K
15. A. Kołodziejczak-Radzimska and T. Jesionowski, *Materials*, **7**, 2833 (2014); https://doi.org/10.3390/ma7042833
16. K.M. Lee, C.W. Lai, K.S. Ngai and J.C. Juan, *Water Res.*, **88**, 428 (2016); https://doi.org/10.1016/j.watres.2015.09.045
17. S. Goktas and A. Goktas, *J. Alloys Compd.*, **863**, 158734 (2021); https://doi.org/10.1016/j.jallcom.2021.158734
18. H.M. Rasheed, K. Aroosh, D. Meng, X. Ruan, M. Akhter and X. Cui, *Mater. Today Energy*, **48**, 101774 (2025); https://doi.org/10.1016/j.mtener.2024.101774
19. M. Mishra and M. Kumar, *Discov. Mater.*, **6**, 26 (2026); https://doi.org/10.1007/s43939-025-00463-9
20. N.H.M. Kaus, A.F. Rithwan, R. Adnan, M.L. Ibrahim, S. Thongmee, and S.F.M. Yusoff, *Catalysts*, **11**, 302 (2021); https://doi.org/10.3390/catal11030302
21. S.I.S. Mashuri, M.F. Kasim, N.H.M. Kaus, Y.H. Tan, A. Islam, U. Rashid, N. Asikin-Mijan, J. Andas, Y.H. Taufiq-Yap, M.K. Yaakob, W.I.N.W. Ismail and M.L. Ibrahim, *Renew. Sustain. Energy Rev.*, **184**, 113602 (2023); https://doi.org/10.1016/j.rser.2023.113602
22. C. Cheng, A. Amini, C. Zhu, Z. Xu, H. Song and N. Wang, *Sci. Rep.*, **4**, 4181 (2014); https://doi.org/10.1038/srep04181
23. D.H. Hanna, D.S. Nady, M.W. Wasef, M.H. Fakhry, F.S. Mohamed, D.M. Isaac, M.M. Kirolos, M.S. Azmy, G.E. Hakeem and C.A. Fathy, *Next Mater.*, **9**, 101275 (2025); https://doi.org/10.1016/j.nxmate.2026.101929
24. H. Singh, M. F. Desimone, S. Pandya, S. Jasani, N. George, M. Adnan, A. Aldarhami, A.S. Bazaid and S.A. Alderhami, *Int. J. Nanomedicine*, **18**, 4727 (2023); https://doi.org/10.2147/IJN.S419369
25. Z. Villagrán, L.M. Anaya-Esparza, C.A. Velázquez-Carriles, J.M. Silva-Jara, J.M. Ruvalcaba-Gómez, E.F. Aurora-Vigo, E. Rodríguez-Lafitte, N. Rodríguez-Barajas, I. Balderas-León and F. Martínez-Esquivias, *Resources*, **13**, 70 (2024); https://doi.org/10.3390/resources13060070
26. C.R. Mendes, G. Dilarri, C.F. Forsan, V.M.R. Sapata, P.R.M. Lopes, P.B. de Moraes, R.N. Montagnolli, H. Ferreira and E.D. Bidoia, *Sci. Rep.*, **12**, 2658 (2022); https://doi.org/10.1038/s41598-022-06657-y
27. S.N. Tan, M.L. Yuen and R.A. Ramli, *Green Anal. Chem.*, **12**, 100230 (2025); https://doi.org/10.1016/j.greeac.2025.100230
28. G. Singh, M.K. Ubhi, K. Jeet, C. Singla and M. Kaur, *Processes*, **11**, 1727 (2023); https://doi.org/10.10.3390/pr11061727
29. D.C. Marcano, D.V. Kosynkin, J.M. Berlin, A. Sinitskii, Z. Sun, A. Slesarev, L.B. Alemany, W. Lu and J.M. Tour, *ACS Nano*, **4**, 4806 (2010); https://doi.org/10.1021/nn1006368
30. A.C.D. Filho, J. de Jesus Soares, M.R.S. Carriço, G.P. Viçozi, W.H. Flores, C.C. Denardin, R. Roehrs and E.L.G. Denardin, *Environ. Sci. Pollut. Res. Int.*, **30**, 36244 (2023); https://doi.org/10.1007/s11356-022-24633-x
31. K. Madi, D. Chebli, H. Ait Youcef, H. Tahraoui, A. Bouguettoucha, M. Kebir, J. Zhang and A. Amrane, *Catalysts*, **14**, 62 (2024); https://doi.org/10.3390/catal14010062
32. A. Negash, S. Mohammed, H.D. Weldekirstos, A.D. Ambaye and M. Gashu, *Sci. Rep.*, **13**, 22234 (2023); https://doi.org/10.1038/s41598-023-48826-7
33. S. Rajakumari, S. Mohandoss and S. Sureshkumar, *Braz. J. Chem. Eng.*, **41**, 1345 (2023); https://doi.org/10.1007/s43153-023-00406-y